Design and Synthesis of Nanostructured Porous SnO2 with High Surface Areas and Their Optical and Dielectric Properties

4 AUTHORS:

Debraj Chandra

Niigata University

39 PUBLICATIONS **532** CITATIONS

SEE PROFILE

Nillohit Mukherjee

Indian Institute of Engineering Science and…

45 PUBLICATIONS **457** CITATIONS

SEE PROFILE

Anup Mondal

Indian Institute of Engineering Science and…

76 PUBLICATIONS **989** CITATIONS

SEE PROFILE

Asim Bhaumik

Indian Association for the Cultivation of Sci…

294 PUBLICATIONS **4,670** CITATIONS

SEE PROFILE

8668

J. Phys. Chem. C **2008,** *112,* 8668–8674

Design and Synthesis of Nanostructured Porous SnO$_2$ with High Surface Areas and Their Optical and Dielectric Properties

Debraj Chandra,[†] Nillohit Mukherjee,[‡] Anup Mondal,[‡] and Asim Bhaumik*,[†]

Department of Materials Science and Centre for Advanced Materials, Indian Association for the Cultivation of Science, Jadavpur, Kolkata 700 032, India, and Department of Chemistry, Bengal Engineering and Science University, Shibpur, Howrah 711103, India

Received: January 29, 2008; Revised Manuscript Received: March 7, 2008

A new structure-directing agent, hexadecyl-2-pyridinyl-methylamine, L$_{16}$, was prepared through Schiff base condensation between pyridine-2-carboxaldehyde and hexadecylamine followed by reduction of the imine with NaBH$_4$. Mesoporous and supermicroporous tin oxide particles with crystalline pore walls were obtained through a low-temperature sol–gel synthesis process by using an anionic surfactant, sodium dodecylsulfate, and hexadecyl-2-pyridinyl-methylamine, respectively, as templates. Powder X-ray diffraction, transmission electron microscopy−energy-dispersive spectrometry, field emission scanning electron microscopy, CHN chemical analysis, N$_2$ sorption, ^{1}H and ^{13}C NMR, high-resolution mass spectrometry, Fourier transform infrared spectroscopy, and UV–vis absorption spectroscopic tools were employed to characterize L$_{16}$ and nanostructured SnO$_2$ materials. X-ray diffraction and transmission electron microscopy image analyses suggested that these porous materials have a wormhole-like disordered arrangement of pores, whereas the pore walls are crystalline. Nitrogen physisorption studies show high specific surface areas up to 555 m^2 g^{-1}, and the uniform nanoscale pore size distribution ranged from supermicropore to mesopores for these materials. These SnO$_2$ materials showed drastic reduction of dielectrics with the induction of porosity vis-à-vis bulk SnO$_2$. These unique optical and electrical properties of porous SnO$_2$ materials over bulk SnO$_2$ could be attributed to the quantum confinement effect.

1. Introduction

Following the discovery of the MCM family of mesoporous silicas using the supramolecular templating approach,[1] mesoporous materials have attracted widespread attention for over a decade because of their fascinating structural diversity, remarkably high surface areas, and narrow pore size distributions. These materials have found huge potential applications in adsorbent,[2] exchanger,[3] catalysis,[4] optical,[5] electrical,[6] medical,[7] sensor,[8] solar cell,[9] and magnetic nanostructure materials.[10] Large numbers of synthetic strategies have been developed, and a variety of materials in terms of both composition and structure have been prepared to meet the ever-increasing demand in this frontier area of science.[11]

On the other hand, the optical and electronic properties of nanostructure materials are strongly influenced by their size, making them a natural bridge between single molecules and bulk materials.[12] Thus, precise control of the morphology together with high specific surface areas, uniform systems of pores, and crystalline pore walls of the semiconducting oxide materials at a nanoscale dimension is highly demanding.[13] Tin oxide, with characteristics like stability toward atmospheric conditions, chemical inertness, mechanical hardness, and high thermal resistance, is very popular among the porous semiconducting oxide materials.[14] SnO$_2$ is a wide-energy-gap n-type semiconductor with a bandwidth of 3.6 eV and has been widely used as a photocatalyst for oxidation of organic compounds and for applications such as solid-state gas sensors, photovoltaics,

and rechargeable lithium batteries, etc.[15] Recently, considerable investigations have been focused on the exploration of novel optical, electrical, and sensing properties of nanocrystalline SnO$_2$.[16,17] The success in many of these applications relies critically on the preparation of crystalline SnO$_2$ with a uniform nanostructure having variable band gaps. As a consequence, synthesis of high surface area porous SnO$_2$ materials with crystalline pore walls and wide band gaps is of great importance.

The concept of utilizing the self-assembled arrays of amphiphiles to synthesize well-ordered mesoporous materials has recently been applied to SnO$_2$[18–20] and related porous materials.[21] Organic structure-directing agents (SDAs) can be suitably designed so that their polar head groups can interact with the inorganic phase through coordination/covalent bonds unlike the conventional ionic or hydrogen-bonding interaction. This could lead to tailored novel nanocomposite materials, which could carry the signatures of both inorganic and organic phases.[22] Thus, a wide range of organic and inorganic phases can be combined to form porous materials having unique electrical, magnetic, and optical properties. As a typical surface-sensitive material, SnO$_2$ has been extensively studied in order to understand the sensing mechanisms and to improve the working performance (i.e., selectivity, sensitivity, and stability).[22] Although the exact reasons that cause the sensing behaviors are still not well-understood, it is accepted that the change in conductivity comes from electron trapping at surface-adsorbed molecules when the sensor is surrounded by oxidizing or reducing atmospheres.[22] Therefore, the use of porous nanostructured SnO$_2$ with large surface-to-volume ratio and small crystal size could lead to easy gas transport and interesting optical and electrical properties. SnO$_2$ nanostructures of different

* To whom correspondence should be addressed. E-mail: msab@iacs.res.in.
† Indian Association for the Cultivation of Science.
‡ Bengal Engineering and Science University.

external morphology[23] have wide applications in device fabrications, especially in photovoltaics.[24]

A simple, yet promising alternative to enhance the catalytic and gas-sensing performance is to control the pore width of the porous materials during the chemical synthesis. In particular, the generation of high specific surface areas, uniform systems of supermicropores,[25] or mesopores with crystalline pore walls[13] and small particle size will result in a higher probability for a substrate to interact with the semiconductor, which is likely to increase the sensitivity of the material. Herein, we report the synthesis of mesoporous and supermicroporous tin oxide particles having a crystalline pore wall through a sol–gel process by using sodium dodecyl sulfate (SDS) and a designed SDA containing two N donors, respectively. These novel materials were characterized by powder X-ray diffraction (XRD), N_2 sorption measurement, thermogravimetric analysis, NMR, Fourier transform infrared (FTIR) spectra, and transmission electron microscopic (TEM) and field emission scanning electron microscopic (FESEM) image analyses. The UV–vis absorption, electrical, and dielectric measurements suggested that these porous materials could be utilized as gas sensors, optoelectronic materials, and as electrodes in solid-state ionic devices.

2. Experimental Section

Synthesis of the Bidentate Structure-Directing Agent. Flame-dried glassware and inert atmospheric conditions were used for the synthesis of this SDA. In a typical Schiff base condensation,[26] a solution of pyridine-2-carboxaldehyde (4.284 g, 0.04 mol) in absolute ethanol (50 mL) was placed under nitrogen in a two-necked round-bottomed flask equipped with condenser and addition funnel. A solution of hexadecylamine (9.658 g, 0.04 mol) in absolute ethanol (50 mL) was added dropwise over 0.5 h. Within 5 min after initiating the addition, the reaction became mildly exothermic. The reaction mixture was kept at reflux 2 h after the completion of the addition of amine. Then, the mixture was allowed to cool to room temperature. $NaBH_4$ (2.269 g, 0.06 mol) was added by pinch to the mixture for 3 h, and the mixture was stirred for 12 h. The mixture was again refluxed for 2 h and cooled to room temperature. Concentrated HCl was added dropwise very carefully until gas evolution completed and the pH was maintained at ∼5–6. Then, 2 N NaOH solution was added to precipitate sodium metaborate while maintaining the pH between 7 and 8 and the mixture was filtered. Then it was extracted three times with 50 mL of chloroform in a separating funnel. Anhydrous Na_2SO_4 (40 g) was added to the filtrate, and the mixture was again filtered. After reducing the volume of the solution in a rotary evaporator, a brownish viscous liquid was obtained, and the as-synthesized SDA was designated as L_{16} (hexadecyl-2-pyridinyl-methylamine).[27] L_{16} can be schematically represented as shown in Figure 1.

Synthesis of Mesoporous and Supermicroporous Tin Oxide. Both the anionic surfactant SDS (Loba Chemie) and bidentate ligand L_{16} were used as SDAs for the synthesis of mesoporous and supermicroporous tin oxide materials, respectively. $SnCl_4 \cdot 5H_2O$ (Loba Chemie) was used as the Sn source in this study. In a typical synthesis, initially required amount of SDA (0.005 mol) was allowed to dissolve in 15 mL of water (for the synthesis with L_{16} instead of water ethanol was used) in ice-cold condition, and the mixture was stirred for 15 min. Then 3.50 g of $SnCl_4$ (0.01 mol) dissolved in 5 mL of water was added to it under continuous stirring for 0.5 h to form a clear solution. After 2 h of constant stirring, tetramethylammonium hydroxide (TMAOH, 25% aqueous, Aldrich) was added
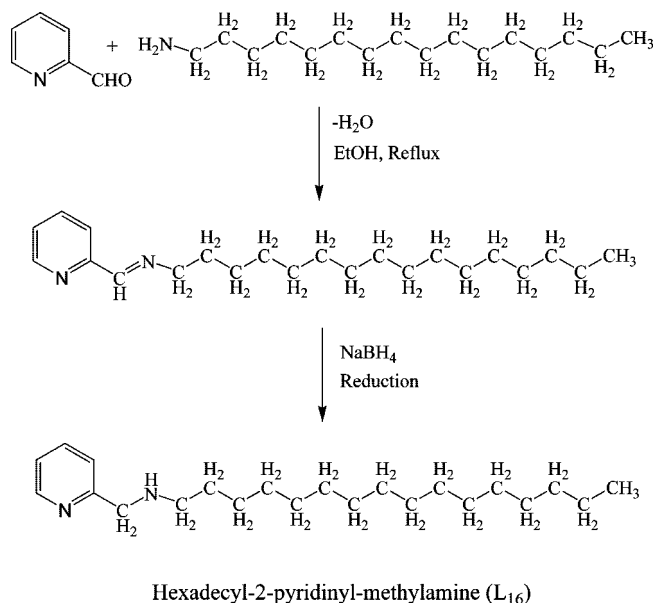
Figure 1. Schematic diagram for the synthesis of bidendate SDA L_{16}.

dropwise and the pH was cautiously maintained at ca. 3.5. The resulting mixture was stirred for another 2 h and then aged in static condition at ice-cold temperature for 24 h. The solid product was recovered by filtration, washed several times with water, and dried under vacuum. Organic SDAs were removed from the as-synthesized solids by two repeated ethanol−HCl extractions at room temperature. The samples synthesized by using SDS and L_{16} are designated as samples 1 and 2, respectively.

Characterization Techniques. X-ray diffraction patterns of the powder samples were obtained with a Seifert P3000 diffractometer using Cu Kα ($\lambda = 0.15406$ nm) radiation. FTIR spectra of these samples were recorded using a Nicolet MA-GNA-FTIR 750 spectrometer series II. Carbon, hydrogen, and nitrogen content were analyzed using a Perkin-Elmer 2400 series II CHN analyzer. Nitrogen adsorption/desorption isotherms were obtained using a Quantachrome Autosorb 1C at 77 K. Prior to gas adsorption, samples were degassed for 2 h at 393 K. Transmission electron microscopic images were recorded in a JEOL 2010 TEM operated at 200 kV. A JEOL JEM 6700F FESEM with an energy-dispersive spectrometer (EDS) attachment was used for the determination of morphology and chemical composition. Thermogravimetry (TG) and differential thermal analysis (DTA) were done in a TA instruments thermal analyzer TA-SDT Q-600. ^1H and ^{13}C NMR experiments were carried out on a Bruker DPX-300 NMR spectrometer. Mass spectrometric data were acquired by the electron spray ionization (ESI) technique using 25–70 eV in a Micromass Q-tof-Micro quadruple mass spectrometer. UV–vis diffuse reflectance spectra were recorded on a Shimadzu UV 2401PC with an integrating sphere attachment. $BaSO_4$ was used as the background standard. The electrical measurements of the samples were carried out by using an Agilent 4284A precision LCR meter. Pellets were made from the powdered samples, and the contacts from the both sides of the pellets were taken by silver paste.

3. Results and Discussion

Characterization of the Bidendate Ligand. ^1H NMR, FTIR, and high-resolution mass spectrometry (HRMS) results for L_{16}[27] suggested the formation of amphiphilic bidentate secondary
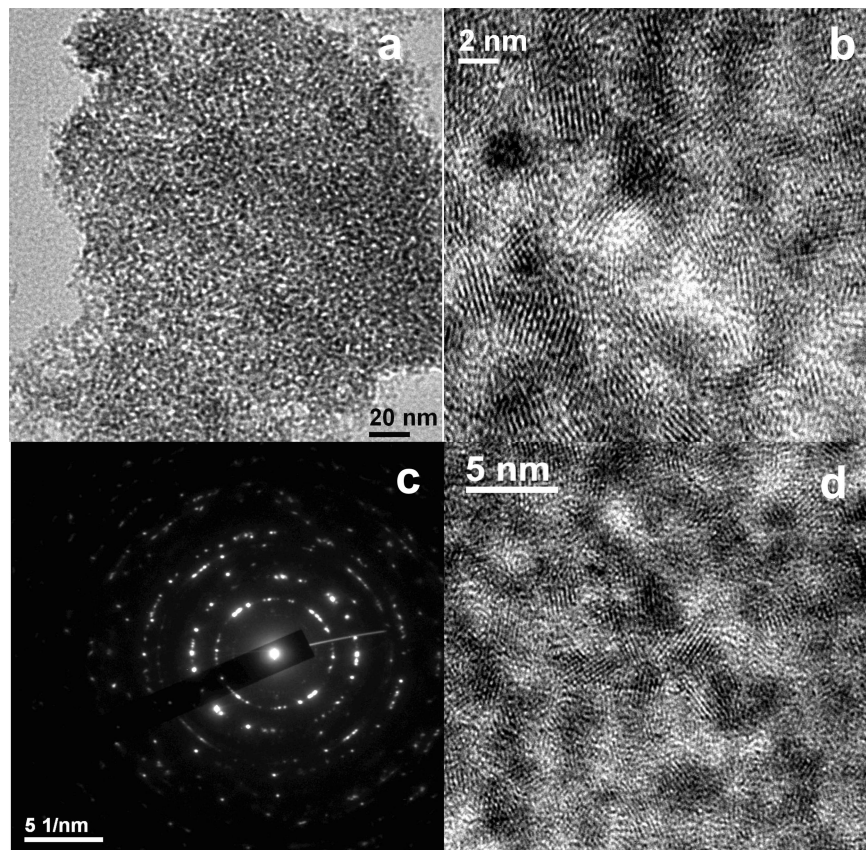
Figure 2. Transmission electron micrographs of sample 1 (a and b), sample 2 (d), and the electron diffraction pattern of sample 1 (c).

amine hexadecyl-2-pyridinyl-methylamine (Figure 1). This Schiff base condensation of the aromatic aldehyde and hexadecyl amine results the long-chain imine in almost quantitative yield. The resulting imine on borohydride reduction yielded the secondary amine L_{16}. N atoms located in the pyridine ring and in the side chain of L_{16} could donate their respective lone pair of electrons to the framework metal ions (i.e., Sn(IV)) and thus could act as an SDA to stabilize the nanostructure.

Electron Microscopy. Representative TEM images at different magnifications and electron diffraction pattern of samples 1 and 2 are shown in Figure 2. In these images (Figure 2, parts a, b, and d), low electron density spots (pores) were seen throughout the specimen and the wormhole-like disordered arrangement of the pores was quite clear for both the samples. A close look into these images suggested the dimension of pores of ca. 2.5 and 1.6 nm, respectively, for samples 1 and 2. On the other hand, from the high-resolution transmission electron microscopy (HRTEM) images (Figure 2, parts b and d) it was clearly observed that high electron density matrixes of the image showed fringes. This was further confirmed from the selected area electron diffraction pattern (Figure 2c) shown for sample 1. In this electron diffraction pattern bright diffraction spots and rings for various crystalline planes were quite clear. This could be attributed as due to the crystalline nature of the pore wall. Particle morphologies of these samples were also examined from FESEM analyses. The electron microscopic images of samples 1 and 2 are shown in Figure 3, top and bottom, respectively. For sample 1 very tiny particles of dimensions 8–10 nm were found to form spherical aggregates of 80–100 nm size particles throughout the specimen. On the other hand, particles of sample 2 were even finer, with the size range of 6–8 nm spherical particles, which did not form large aggregates. The morphological features of these mesoporous and supermicroporous tin oxide
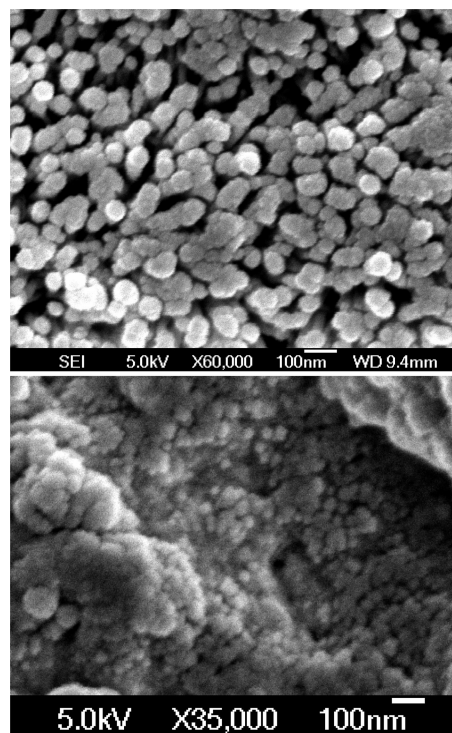
Figure 3. SEM images of samples 1 (top) and 2 (bottom).

samples were quite uniform and consistent and suggested the formation of nanosize particles for both of the samples.

Powder XRD. Small-angle powder XRD patterns of as-synthesized powder samples 1 (a) and 2 (c) and extracted powder samples 1 (b) and 2 (d) (Supporting Information, S1, A) show a single major diffraction peak at low 2θ for the d

Nanostructured Porous SnO$_2$

J. Phys. Chem. C, Vol. 112, No. 23, 2008 **8671**

TABLE 1: Physico−Chemical Properties of Porous SnO$_2$ Materials

sample no.	SDA used	BET surface area (m^2 g^{-1})	pore width (nm)	pore volume (cm^3 g^{-1})	d spacing (nm)^a		wall thickness (nm)	pore width^b
					as-synthesized	extracted		
1	SDS	555	2.56	0.57	4.64	3.70	1.14	2.7
2	L$_{16}$	398	1.61	0.29	2.81	2.64	1.03	1.5

^{a} Obtained from powder XRD data. ^{b} Average value obtained from TEM image analysis.

plane corresponding to the disordered mesophases. No distinctive higher order reflexes were observed in either of the samples. The d spacings of as-synthesized and extracted mesostructures of sample 1 are 4.6 and 3.7 nm, respectively, as calculated from the maximums of the XRD patterns, which are also consistent with the pore center to pore center correlation lengths as determined from the TEM micrographs. The wide-angle XRD patterns (Supporting Information, S1, B) of the as-synthesized samples 1 and 2 reveal that both these mesoporous and supermicroporous tin oxide materials are polycrystalline in nature and planes corresponding to (110), (101), (211), and (112) are clearly observed (JCPDS card no. 41-1445). All other peaks corresponding to other planes appeared with very weak intensities. The presence of broad and weak peaks indicates that SnO$_2$ has a very small crystalline size or that SnO$_2$ particles are semicrystalline in nature.[13] The HRTEM image and electron diffraction (ED) pattern also support the crystalline nature of the pore wall, as observed from wide-angle XRD patterns. Particle sizes of our mesoporous and supermicroporous SnO$_2$ samples were measured from the full width at half-maximum (fwhm) of the small-angle peaks using Scherrer's equation ($D = 0.9\lambda/(\beta \cos \theta)$). The particle sizes measured from these powder XRD patterns for samples 1 and 2 were 8.7 and 6.3 nm, respectively. These values agree well with the electron microscopic data (Figure 3). It is pertinent to mention that there are reports on the mesostructured SnO$_2$ by using SDS as the template.[28] However, the SnO$_2$ mesostructure was collapsed during the removal of the template, and thus no attempt was made to explore the porosity and BET surface area of that material.

N$_2$ Sorption. N$_2$ adsorption/desorption isotherms at 77 K (Supporting Information, S2) for sample 1 could be classified as a type IV isotherm characteristic of the mesoporous materials, whereas that for sample 2 could be classified as a type I isotherm characteristic of microporous materials. In these isotherms between P/P_0 of 0.025–0.42 the adsorption amount gradually increases for sample 1, unlike capillary condensation and hysteresis at high P/P_0 as usually observed for mesopores.[29] On the other hand, for sample 2, the adsorption amount reaches a plateau at $P/P_0 = 0.12$ corresponding to a typical microporous solid. The BET surface areas for the acid-extracted samples 1 and 2 were 555 and 398 m^2 g^{-1}, respectively. Physico−chemical properties of these samples are given in Table 1. Pore size distributions of these samples employing the NLDFT[30] method (N$_2$ adsorption on silica as reference) also (Supporting Information, S2) suggested that sample 2, synthesized by using L$_{16}$ SDA, has relatively smaller specific surface area as well as smaller average pore width than sample 1, synthesized using SDS. This result suggested that bidentate SDA L$_{16}$ was bound with the Sn(IV) moieties present in the framework during synthesis. Pore widths and wall thicknesses obtained from powder XRD and N$_2$ sorption data for both the samples agree well with those values obtained from TEM image analyses (Table 1). The effective pore width of this SnO$_2$ material synthesized with L$_{16}$ was 1.61 nm, which could be classified as supermicroporous (pore diameter falls within the 1.0−2.0 nm range).[25] Acid ethanol extraction could help to remove the SDAs almost

completely and thus generate porosity. To the best of our knowledge the supermicroporous and mesoporous tin oxide materials reported herein have much higher specific surface area compared to other related porous tin oxide materials reported so far.[18–20] Unlike our synthesis of mesoporous TiO$_2$ using a designed template,[26b] where the carbonyl moiety of salicaldehyde was used during condensation, here pyridine-2-carboxaldehyde was used, and the resulting bidentate ligand L$_{16}$ could be easily removed from the as-synthesized material to generate the novel supermicroporous SnO$_2$ material with crystalline pore walls. It is pertinent to mention here that supermicroporous SnO$_2$ has not been reported yet, and due to its unique pore architecture and high surface area it has a large potential to be used as a selective adsorbent.

Thermal Analyses. The quantitative determination of the framework stability upon heat treatment of these surfactant-free nanoporous tin oxide materials was estimated by TG and DTA under N$_2$ flow. The TG analyses of these samples showed a first weight loss at up to 373 K due to desorption of physisorbed water (about 8.0 wt %; Supporting Information, S3). This is followed by a gradual decrease in the weight in the temperature range of 373−773 K, by two steps, which corresponds to the loss of a trace amount of organic surfactant present in the mesoporous SnO$_2$ material. No significant weight loss was observed above 773 K. It is interesting to note that weight loss in the range of 373−773 K is a little lower for sample 1 compared to sample 2. To study the thermal stability under air for these mesoporous and supermicroporous SnO$_2$ materials we have heated the template-free samples at four different temperatures (473, 523, 573, and 623 K) in the presence of air. The powder XRD patterns of sample 1 heated at 473–623 K (Supporting Information, S4) suggested that up to 573 K no significant change in the XRD pattern was observed compared to that observed at room temperature (Supporting Information, S1A and B). But further increase in temperature to 623 K decreases the peak intensity considerably. Sample 2 followed an identical behavior. This result suggested that our porous SnO$_2$ samples are stable up to ca. 573 K. To study the change of particle size during this heat treatment we have carried out the SEM analysis of sample 1 heat-treated at 573 K. It has been clearly seen from the SEM image (Supporting Information, S5) that small particles of ca. 20–30 nm have been assembled to form very large aggregated particles during heat treatment. Thus, while heating up to 573 K the mesopores/supermicropores and the pore walls have retained their disordered features during the enlarging of the tiny SnO$_2$ particles.

FTIR Spectroscopy. FTIR spectra of different as-synthesized samples (Supporting Information, S6) suggested that, apart from the C−H vibrations at ca. 2845 and 2925 cm^{-1}, different bending vibrations of N−H and N−C bonds between 1600 and 600 cm^{-1} were observed for as-synthesized samples, whereas these peaks are almost absent for the acid-extracted samples (Supporting Information, S6). From the spectra it is clear that acid extraction procedure is quite efficient to remove almost all of the organic SDA from the solid matrixes. The broad band observed at ca. 650 cm^{-1} for all the samples corresponds to Sn−O stretching. This result is in agreement with data from
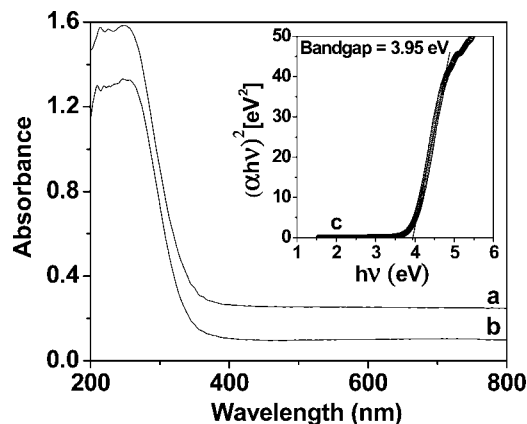
Figure 4. UV–vis diffuse reflectance spectra of SDA-free powder samples 1 (a) and 2 (b). The direct band gap calculated from the absorbance value for sample 1 (c) is shown in the inset.
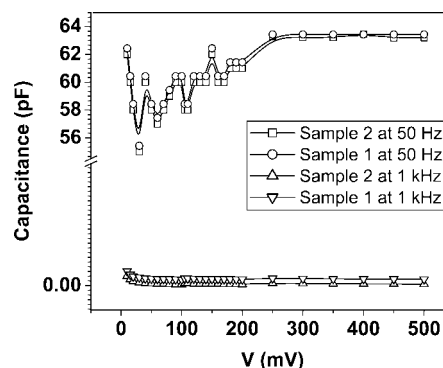

Figure 5. Alternating current–voltage plots of samples 1, 2, and bulk SnO_2 under 50 Hz and 1 KHz fields.

Figure 6. Alternating current capacitance–voltage plot of samples 1 and 2 under 50 Hz and 1 KHz fields.

literature.[31] Bands at ca. 1630 and 3430 cm^{-1} could be assigned as due to H–OH stretching and physisorbed water O–H bond vibration modes, respectively.

UV–Vis Absorption. UV–vis spectroscopy was used to characterize the optical absorbance as well as band gap energies of these porous tin oxide materials. Figure 4 shows the UV–vis absorption spectrum of extracted samples 1 and 2. Optical band gaps were calculated from the absorbance data by plotting $(\alpha h\nu)^2$ versus $h\nu$ and extrapolating the linear portion of the curve to $(\alpha h\nu)^2 = 0$, where α is the absorption coefficient and $h\nu$ is the photon energy. It can be seen that the absorption band edge for both of these samples is at ca. 320 nm and the direct band gap (E_g) measured from the absorbance value for the extracted samples is 3.95 eV (shown in the inset), which is much larger than that of the bulk SnO_2 ($E_g = 3.6$ eV).[14,32] For semiconductor nanocrystals a blue-shift in the absorption spectra is attributed to the quantum confinement effect,[33] where the size of the SnO_2 nanoparticles is smaller than the Bohr exciton radius of SnO_2 (ca. 2.7 nm). The electron microscopic images as well as powder XRD data revealed the particle size of both samples varied from 6 to 9 nm, with pore diameters varying from 1.6 to 2.5 nm. Here in these mesoporous and supermicroporous SnO_2 materials pore walls can be considered as being composed of nanosize molecular clusters.[33a] The wall thicknesses for these mesoporous and supermicroporous SnO_2 materials are (Table 1) much smaller than the Bohr excitonic radius of SnO_2. As a result, the effective gap between the valence band and conduction band increased, causing a blue-shift in the band gap. These further cause nonstoichiometry and defects at the porous SnO_2 surface resulting in low coordination of SnO_2 in particles. This accounts for the unusual optical properties of these mesoporous and supermicroporous SnO_2 nanostructured materials.

Electrical Measurements (ac). The electrical measurements of these porous tin oxide materials were carried out in the solid state at room temperature. The electrical properties of a bulk tin oxide synthesized by employing the same reaction condition but without addition of SDA are shown for comparison. Pellets were made from the powdered samples, and the contacts from both sides of the pellets were taken by silver paste. Figures 5 and 6 represent ac current–voltage (I–V) and capacitance–voltage (C–V) plots of these samples, respectively, under two different fixed fields of 50 Hz and 1 KHz. From the I–V data under the 50 Hz field for extracted samples 1 and 2, a stepwise increase in current was observed between 0 and 200 mV showing nonohmic behavior, but with increasing the external bias from 250 mV onward, the I–V plot becomes linear under
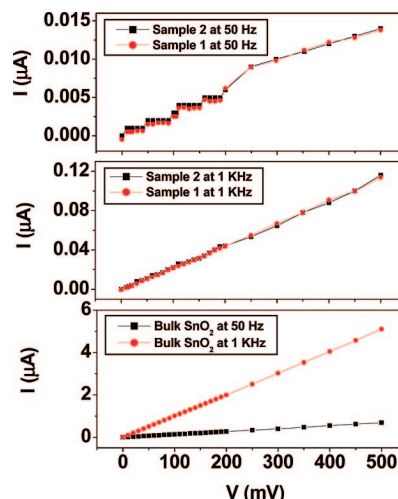
higher potential values. On the other hand, the bulk SnO_2 shows a typical linear I–V characteristic from the beginning under the 50 Hz field. This nonlinear nature of the I–V plot might be due to the tunneling effect.[34,35] Since these two tin oxide samples are highly porous and have small particle sizes, these materials can be regarded as an assembly of many nanocapacitors made up of nanopores and tin oxide nanoparticles (pore walls). Thus, there is a great chance of electron entrapment inside these pores and particle boundaries, which in turn creates electron-trapping zones of different energy levels. At a certain potential, the electrons that previously occupied the trapping levels get released, which is reflected in the sharp rise in current. The presence of different trapping zones with different energy levels can be assumed from the multistep I–V characteristics under the 50 Hz field. Since these kinds of trapping zones are absent in bulk nonporous SnO_2 it showed a typical linear I–V characteristic. These nonlinear phenomena were again observed during C–V measurements for these nanoporous materials at lower potential values (up to 200 mV) under the 50 Hz field due to the release of trapped charges from different trapping zones as was explained earlier. The bias levels, at which the trapped charges are released, a fall in capacitance is observed. Again, on increasing the ac frequency to 1 kHz, the I–V and C–V plots become linear, indicating that the trapping zones were no longer capable of holding on the trapped charges and all the trapped charges were released simultaneously even at the low potential value.

Resistivity Measurements. A typical exponential decay of resistivity was observed when the frequency is plotted against

Nanostructured Porous SnO$_2$

J. Phys. Chem. C, Vol. 112, No. 23, 2008 **8673**
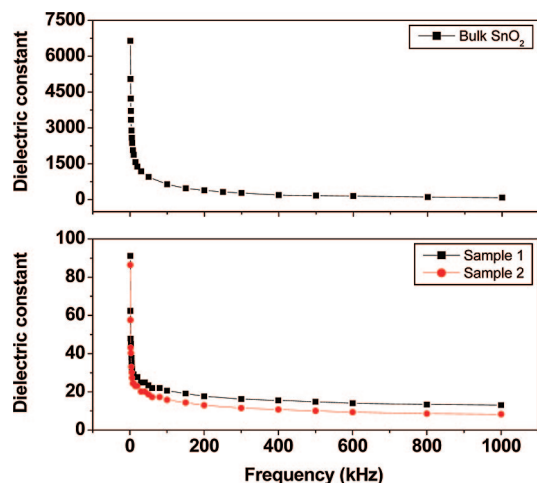
Figure 7. Dielectric constant against frequency plots of samples 1 and 2 and bulk SnO$_2$.

resistivity for these nanoporous tin oxide samples as well as that of bulk SnO$_2$. The resistivity of these nanoporous materials was very high (about 100 times) compared to that of the bulk SnO$_2$ matrix. This is again due to the presence of pores with nanoscale dimensions and its uneven distribution, where the free movement of electrons is restricted to a large extent.[35] When a potential is applied across our sample, an electron first has to travel through the sample resulting in the initial sample resistance. After this process, the electron can become trapped at a grain boundary capacitor or travel through a resistive grain boundary. Because of the unique nanostructure of these materials the electron can also associate with the boundary of a pore, producing a pore resistance. Because of pore resistance as well as particle boundary resistance, the resistivity of these nanoporous tin oxide materials is very high compared to that of bulk SnO$_2$. The high resistivity values of the porous samples are responsible for the low current observed in the *I–V* measurements. It is pertinent to note that the value of current shown by samples 1 and 2 at 500 mV bias under 50 Hz is about 0.014 μA which increases approximately 10 times, i.e., to 0.12 μA under 1 kHz. But, the bulk SnO$_2$ material at 500 mV bias showed about 0.7 and 5.0 μA current under 50 Hz and 1 kHz fields, respectively. The comparatively low current output showed by these nanoporous tin oxides for a given condition is due to their highly porous nature of the SnO$_2$ surface.

Dielectric Measurements. In Figure 7 the dielectric constants were plotted against frequencies for bulk SnO$_2$ synthesized in the absence of any SDA and samples 1 and 2. From the plot it is clear that these porous SnO$_2$ materials have a low dielectric constant (about 100 times lower) compared to that of the bulk material at any particular point of frequency. This might be due to the fact that the number of nanoparticles of SnO$_2$, which could act as the nanodipoles, present per unit volume for the porous materials is low, compared to that of the bulk one. Due to the highly porous nature of the matrix of samples 1 and 2, there occurs a significant amount of void space, which in turn lowers the number of SnO$_2$ units per unit volume.[36] Further, the orientation of the effective SnO$_2$ units for samples 1 and 2 under a particular frequency is also not so uniform like that of the bulk SnO$_2$ matrix, which acts as a continuous system, and could also be responsible for the comparatively low dielectric constants for samples 1 and 2.

Structure-Directing Role of SDS and L$_{16}$. Here mesoporous and supermicroporous SnO$_2$ materials were synthesized through a sol–gel process using the anionic surfactant SDS and neutral

bidentate L$_{16}$ as SDAs. For sample 1 synthesized by using SDS, electrostatic interaction can take place between the negatively charged head groups of the supramolecular micelle of the anionic surfactants and the oppositely charged inorganic species (positively charge Sn^{4+} metal ion) in solution, following the templating pathway for other related mesoporous materials.[37,38] For sample 2 the organic SDA (L$_{16}$) has been suitably designed so that its polar head groups will interact with the inorganic phase through a coordination bond. Here L$_{16}$ could interact with the cationic Sn^{4+} species in solution through the donor nitrogen atom of the pyridine and aliphatic secondary amine (–NH–) groups similar to that observed for mesoporous titanium composites synthesized by Schiff base ligands.[26a] The hydrophobic tail present in the surfactant/ligand may help to generate the supramolecular assembly and void space inside the pores.

4. Conclusions

Condensation of pyridine-2-carboxaldehyde with a long-chain primary amine, hexadecylamine, followed by the reduction of the imine adduct, yielded a bidentate SDA having two N-donor sites. We have prepared new supermicroporous and mesoporous tin oxide materials having crystalline pore walls through this tailor-made SDA and anionic surfactant SDS, respectively, employing a low-temperature synthesis method. These novel nanoporous SnO$_2$ materials have very high specific surface area and display some interesting optical, electrical, and dielectric properties at room temperature. The pore walls of these porous SnO$_2$ materials can be considered as being composed of nanoclusters of dimension less than ca. 2.7 nm. The blue-shift of the absorption edge in these materials may originate from the confinement of electrons and holes (quantum size effect) in the defect levels of the band gap. The interesting morphological features of these materials with small particle sizes together with high specific surface areas, uniform systems of nanopores, and crystalline pore walls could lead to many potential applications especially in low dielectric, optoelectronic, and sensor applications.

Supporting Information Available: Figures S1–S6, powder XRD, N$_2$ sorption, TG–DTA, XRD, and SEM at 573 K, and FTIR, respectively. This material is available free of charge via the Internet at http://pubs.acs.org.

References and Notes

(1) Kresge, C. T.; Leonowicz, M. E.; Roth, W. J.; Vartuli, J. C.; Beck, J. S. *Nature* **1992**, *359*, 710–712.

(2) (a) Mercier, L.; Pinnavaia, T. J. *Adv. Mater.* **1997**, *9*, 500–503. (b) Kruk, M.; Jaroniec, M. *Chem. Mater.* **2001**, *13*, 3169–3183.

(3) Bhaumik, A.; Inagaki, S. *J. Am. Chem. Soc.* **2001**, *123*, 691–696.

(4) (a) Garro, R.; Navarro, M. T.; Primo, J.; Corma, A. *J. Catal.* **2005**, *233*, 342–350. (b) Gomez, S.; Garces, L. J.; Villegas, J.; Ghosh, R.; Giraldo, O.; Suib, S. L. *J. Catal.* **2005**, *233*, 60–67.

(5) (a) Scott, B. J.; Wirnsberger, G.; Stucky, G. D. *Chem. Mater.* **2001**, *13*, 3140–3150. (b) Qi, Z.-M.; Honma, I.; Zhou, H. *J. Phys. Chem. B* **2006**, *110*, 10590–10594.

(6) Sasidharan, M.; Mal, N. K.; Bhaumik, A. *J. Mater. Chem.* **2007**, *17*, 278–284.

(7) (a) Vallet-Regí, M. *Dalton Trans.* **2006**, 5211–5224. (b) Jiao, F.; Harrison, A.; Jumas, J. C.; Chadwick, A. V.; Kockelmann, W.; Bruce, P. G. *J. Am. Chem. Soc.* **2006**, *128*, 5468–5474.

(8) (a) Evans, S. A. G.; Elliott, J. M.; Andrews, L. M.; Bartlett, P. N.; Doyle, P. J.; Denuault, G. *Anal. Chem.* **2002**, *74*, 1322. (b) Casasús, R.; Aznar, E.; Marcos, M. D.; Martínez-Máñez, R.; Sancenón, F.; Soto, J.; Amorós, P. *Angew. Chem., Int. Ed.* **2006**, *45*, 6661. (c) Wagner, T.; Kohl, C.-D.; Fröba, M.; Tiemann, M. *Sensors* **2006**, *6*, 318.

(9) Bach, U.; Lupo, D.; Comte, P.; Moser, J. E.; Weissortel, F.; Salbeck, J.; Spreitzer, H.; Gratzel, M. *Nature* **1998**, *395*, 583–585.

(10) Delahaye, E.; Escax, V.; El Hassan, N.; Davidson, A.; Aquino, R.; Dupuis, V.; Perzynski, R.; Raikher, Y. L. *J. Phys. Chem. B* **2006**, *110*, 26001–26011.

(11) (a) Kim, T.-W.; Ryoo, R.; Kruk, M.; Gierszal, K. P.; Jaroniec, M.; Kamiya, S.; Terasaki, O. *J. Phys. Chem. B* **2004**, *108*, 11480–11489. (b) Naik, S. P.; Yokoi, T.; Fan, W.; Sasaki, Y.; Wei, T. C.; Hillhouse, H. W.; Okubo, T. *J. Phys. Chem. B* **2006**, *110*, 9751–9754.

(12) (a) Jortner, J.; Rao, C. N. R. *Pure Appl. Chem.* **2002**, *74*, 1489. (b) Schmidt, G. *Nanoparticles: From Theory to Application*; Wiley-VCH: Weinheim, 2004.

(13) (a) Yang, P.; Zhao, D.; Margolese, D. I.; Chmelka, B. F.; Stucky, G. D. *Nature* **1998**, *396*, 152–155. (b) Brezesinski, T.; Erpen, C.; Iimura, K.-I.; Smarsly, B. *Chem. Mater.* **2005**, *17*, 1683–1690. (c) Lu, D.; Katou, T.; Uchida, M.; Kondo, J. N.; Domen, K. *Chem. Mater.* **2005**, *17*, 632–637.

(14) Fujihara, S.; Maeda, T.; Ohgi, H.; Hosono, E.; Imai, H.; Kim, S.-H. *Langmuir* **2004**, *20*, 6476–6481.

(15) (a) Kuang, Q.; Lao, C.; Wang, J. L.; Xie, Z.; Zheng, L. *J. Am. Chem. Soc.* **2007**, *129*, 6070–6071. (b) Vilaca, G.; Jousseaume, B.; Mahieus, C.; Belin, C.; Cachet, H.; Bernard, M. C.; Vivier, V.; Toupance, T. *Adv. Mater.* **2006**, *18*, 1073–1077. (c) Kim, C.; Noh, M.; Choi, M.; Cho, J.; Park, B. *Chem. Mater.* **2005**, *17*, 3297–3301.

(16) (a) Kim, T. W.; Lee, D. U.; Yoon, Y. S. *J. Appl. Phys.* **2000**, *88*, 3759. (b) Jeong, J.; Choi, S. P.; Chang, C. I.; Shin, D. C.; Park, J. S.; Lee, B.-T.; Park, Y.-J.; Song, H.-J. *Solid State Commun.* **2003**, *127*, 595.

(17) (a) Chen, Z. W.; Lai, J. K. L.; Shek, C. H. *Phys. Rev. B* **2004**, *70*, 165314. (b) Gu, F.; Wang, S. F.; Lu, M. K.; Cheng, X. F.; Liu, S. W.; Zhou, G. J.; Xu, D.; Yuan, D. R. *J. Cryst. Growth* **2004**, *262*, 182–185.

(18) (a) Severin, K. G.; Abdel-Fattah, T. M.; Pinnavaia, T. J. *Chem. Commun.* **1998**, 1471–1472. (b) Chen, F.; Liu, M. *Chem. Commun.* **1999**, 1829–1830.

(19) (a) Urade, V. N.; Hillhouse, H. W. *J. Phys. Chem. B* **2005**, *109*, 10538–10541. (b) Velasquez, C.; Rojas, F.; Esparza, J. M.; Ortiz, A.; Campero, A. *J. Phys. Chem. B* **2006**, *110*, 11832–11837.

(20) (a) Wang, Y.; Ma, C.; Sun, X.; Li, H. *Microporous Mesoporous Mater.* **2001**, *49*, 171–178. (b) Wang, Y.-D.; Ma, C.-L.; Wu, X.-H.; Sun, X.-D.; Li, H.-D. *Sens. Actuators, B* **2002**, *85*, 270–276.

(21) (a) Srivastava, D. N.; Chappel, S.; Palchik, O.; Zaban, A.; Gedanken, A. *Langmuir* **2002**, *18*, 4160–4164. (b) Hyodo, T.; Abe, S.; Shimizu, Y.; Egashira, M. *Sens. Actuators, B* **2003**, *93*, 590–600.

(22) Batzill, M.; Katsiev, K.; Burst, J. M.; Diebold, U.; Chaka, A. M.; Delley, B. *Phys. Rev. B* **2005**, *72*, 165414.

(23) Liu, Y.; Dong, J.; Liu, M. L. *Adv. Mater.* **2004**, *16*, 353–356.

(24) Kamat, P. V.; Barazzouk, S.; Thomas, K. G.; Hotchandani, S. *J. Phys. Chem. B* **2000**, *104*, 4014–4017.

(25) (a) Mal, N. K.; Fujiwara, M. *Chem. Commun.* **2002**, 2702–2703. (b) Shpeizer, B. G.; Bakhmutov, V. I.; Clearfield, A. *Microporous Mesoporous Mater.* **2006**, *90*, 81–86.

(26) (a) Chandra, D.; Bhaumik, A. *Microporous Mesoporous Mater.* **2007**, *101*, 348–354. (b) Chandra, D.; Yokoi, T.; Tatsumi, T.; Bhaumik, A. *Chem. Mater.* **2007**, *19*, 5347–5354.

(27) NMR, FTIR, and HRMS for L$_{16}$. ^{1}H NMR (300 MHz, CDCl$_3$) δ 0.88 (t, *J* = 6.8 Hz, 3H), 1.18–1.40 (m, 26H), 1.51–1.59 (m, 2H), 2.67 (t, *J* = 7.3 Hz, 2H), 3.93 (s, 2H), 7.15 (dd, *J* = 5.1, 6.9 Hz, 1H), 7.32 (d, *J* = 8.0 Hz, 1H), 7.63 (t, *J* = 6.9 Hz, 1H), 8.55 (d, *J* = 5.1 Hz, 1H); ^{13}C NMR (75 MHz, CDCl$_3$) δ 14.2, 22.7, 27.4, 29.4, 29.6 (2C), 29.7 (7C), 29.9, 32.0, 49.6, 55.1, 122.0, 122.5, 136.5, 149.3, 159.4. IR (neat) 3311, 2923, 2852, 1591, 1465, 1433, 1126, 754 cm^{-1}. HRMS: calcd for C$_{22}$H$_{41}$N$_2$ [M$^+$ + H], 333.3269; found, 333.3265.

(28) Qi, L.; Ma, J.; Cheng, H.; Zhao, Z. *Langmuir* **1998**, *14*, 2579–2581.

(29) Sing, K. S. W.; Everett, D. H.; Haul, R. A. W.; Moscou, L.; Pierotti, R. A.; Rouquerol, J.; Siemieniewska, T. *Pure Appl. Chem.* **1985**, *57*, 603–619.

(30) Vishnyakov, A.; Russo, R.; Neimark, A. V.; Ravikovitch, P. I. *Langmuir* **2000**, *16*, 2311–2320.

(31) Patil, P. S.; Kawar, R. K.; Seth, T.; Amalnerkar, D. I.; Chigare, P. S. *Ceram. Int.* **2003**, *29*, 725.

(32) (a) Sanon, G.; Rup, R.; Mansingh, A. *Thin Solid Films* **1990**, *190*, 287–301. (b) Ying, Z.; Wan, Q.; Song, Z. T.; Feng, S. L. *Nanotechnology* **2004**, *15*, 1682–1684.

(33) (a) Kamat, P. V. *Chem. Rev.* **1993**, *93*, 267–300. (b) Kim, T. W.; Lee, D. U.; Yoon, Y. S. *J. Appl. Phys.* **2000**, *88*, 3759. (c) Law, M.; Sirbuly, D. J.; Johnson, J. C.; Goldberger, J.; Saykally, R. J.; Yang, P. *Science* **2004**, *305*, 1269–1273. (d) Gu, F.; Wang, S. F.; Lu, M. K.; Zhou, G. J.; Xu, D.; Yuan, D. R. *J. Phys. Chem. B* **2004**, *108*, 8119–8123. (e) Gu, F.; Wang, S. F.; Lu, M. K.; Cheng, X. F.; Liu, S. W.; Zhou, G. J.; Xu, D.; Yuan, D. R. *J. Cryst. Growth* **2004**, *262*, 182–185. (f) Wang, G.; Lu, W.; Li, J.; Choi, J.; Jeong, Y.; Choi, S. Y.; Park, J.-B.; Ryu, M. K.; Lee, K. *Small* **2006**, *2*, 1436–1439.

(34) Korlann, S. D.; Riley, A. E.; Kirsch, B. L.; Mun, B. S.; Tolbert, S. H. *J. Am. Chem. Soc.* **2005**, *127*, 12516–12527.

(35) Feng, Y.; Yao, R.; Zhang, L. *Physica B* **2004**, *350*, 348–352.

(36) Ghosh, P. K.; Mitra, M. K.; Chattopadhyay, K. K. *Nanotechnology* **2005**, *16*, 107–112.

(37) Che, S.; Garcia-Bennett, A. E.; Yokoi, T.; Sakamoto, K.; Kunieda, H.; Terasaki, O.; Tatsumi, T. *Nat. Mater.* **2003**, *2*, 801–805.

(38) Mohamed, M. M.; Bayoumy, W. A.; Khairy, M.; Mousa, M. A. *Microporous Mesoporous Mater.* **2006**, *97*, 66–77.